Journal of Engineering Science and Technology
Vol. 19, No. 5 (2024) 1794 - 1810

A PQ CONTROL STRATEGY USING FLATNESS-BASED THEORY FOR THE THREE-PHASE FOUR-WIRE GRID-CONNECTED INVERTER IN AN AC BATTERY

TUAN ANH DO[1,2], QUANG NGHIA LE[1],
QUANG DICH NGUYEN[2], PHUONG VU[1]

[1]School of Electrical and Electronic Engineering, Hanoi University of Science and Technology, Hanoi, 100000, Vietnam
[2]Institute for Control Engineering and Automation, Hanoi University of Science and Technology, Hanoi, 100000, Vietnam
*Corresponding Author: phuong.vuhoang@hust.edu.vn

Abstract

In a multi-functional AC battery, power control is the key to performing many functions such as reactive power compensation, active power filter, and point of common coupling (PCC) voltage control. It is very important to develop a control strategy that ensures a fast dynamic response and still maintains good tracking performance to help stabilize the system under severe conditions. To meet these requirements, a PQ control structure for the three-phase four-wire grid-connected inverter in a synchronous reference frame based on flatness theory is proposed. The active and reactive power is indirectly controlled via a current control loop using the instantaneous power theory, and then the PCC voltage can be regulated by the reactive power compensation. The feasibility of the study is proved and validated by the real-time simulation results.

Keywords: Battery energy storage system, Flatness-based theory, PQ control, point of common coupling, Three-phase four-wire converter.

1. Introduction

Developing renewable energy is becoming a worldwide trend. Much research has been done to optimize various aspects of the energy transfer process from these sources to household loads and industrial loads. However, this renewable energy source has a major drawback, which is its availability. For example, in household applications, during the day the amount of power required from the loads is relatively low and the capacity that can be provided from renewable energy sources (solar, wind power, etc.) is relatively high.

At night, the process happens in reverse, the capacity from the renewable energy sources cannot provide enough for the increased load demand. This leads to an overabundance in terms of energy supply during the day and a lack of energy supply during the night. To solve this problem, an energy storage system (ESS) was introduced [1-3]. An energy storage system allows storing excess energy from renewable energy sources (or the grid) onto a storage device when the load power demand is less than that can be mobilized at the sources.

Conversely, when the required power from the load is greater than that can be generated from the sources, part of the energy from ESS will be extracted to compensate for the shortfall. There are many types of ESS, which are classified by their storage options: batteries, thermal or mechanical systems. In the context of this study, the authors' primary focus is battery energy storage systems, specifically emphasizing the utilization of second-life batteries [4].

In this research, the AC-coupled topology is selected for home battery storage systems, which are available to connect to the installed solar home. This application was first introduced by Tesla as an AC Battery, which commonly consists of a two-stage power converter and the battery as shown in Fig. 1.

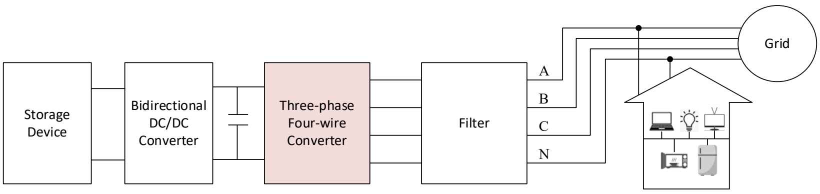

Fig. 1. Structure of an AC battery using the three-phase four-wire topology.

The Power Factor Correction (PFC) stage directly controls the amount of power injected/absorbed to/from the grid and the bidirectional DC/DC stage is responsible for the charge profile of the storage device. Based on the PQ control theory, the AC Battery can be further utilized to perform more functions simultaneously such as reactive power compensation, active filter, point of common coupling voltage control, etc., to support the power grid under non-ideal conditions to meet grid requirements, hence referring as the Multi-functional Battery Energy Storage System in [5-7].

The PFC stage plays an important role in the AC Battery so that the grid current is in phase with the grid voltage and its total harmonic distortion meets the IEEE519 standard. The selected power topology should be able to adapt to different grid conditions and have high efficiency with a compact size. For the three-phase grid network, the Three-phase Four-wire topology are getting a lot more attention recently due to its ability to deal with the case of non-ideal grid or loads by regulating the neutral current through the fourth branch [8].

The size of the PFC power circuit can still be ensured even with the addition of a MOSFET branch based on the Silicon Carbide (SiC) technology which helps to increase the power density and offer higher switching frequency [8].

As can be seen above, power control is the key to a multi-functional AC Battery. The control structure must be designed to ensure fast and accurate dynamic response in real-time control and well-adapt under abnormal grid conditions. Many previous publications have suggested different control strategies for both single- and three-phase power grids. A control structure for multi-functional EV chargers in a single-phase grid system was introduced. [9, 10]. A novel smart inverter in which a PV inverter can be controlled to perform dynamic reactive power compensation and PCC voltage regulation on a 24/7 basis for the three-phase grid is proposed [11].

To guarantee that the microgrid operates well in both islanded and grid-connected modes, the VF control regulates the voltage and frequency of each power converter connected to each distributed generation in the islanded mode while the P-Q control regulates the output active and reactive powers of each distributed generation in the grid-connected mode [12]. Some recent works have studied the optimal voltage control strategy, such as the robustness control with a discrete-time sliding mode current controller [13] or the P-Q control-based Particle swarm optimization theory [14].

Moreover, the dynamic response in these strategies is another important issue and some nonideal cases show sluggish performance. To deal with linear regulator limitations, several nonlinear control methods are proposed in the literature including feedback linearization control [15] or backstepping control [16]. These control methods use differentiation to achieve the control law, which results in high-order derivative control terms. These derivatives can affect the control law capabilities under severe load disturbances and model inaccuracies.

Among the reported control strategies, flatness-based control (FBC) appears as an interesting nonlinear control approach due to its useful performance when explicit trajectory planning is required under different operating conditions. Indeed, the flatness theory allows an accurate description of the transient and steady-state dynamics of the overall system state variables based on differentially flat outputs. In addition, and as reported in various works [17, 18], the FBC demonstrates stable performances even under large operating points and system parameter variations.

In this paper, a control strategy based on flatness-based theory for PQ control for a three-phase four-wire grid-connected inverter is proposed. The output vector consists of DC link voltage, q-axis, and 0-axis components of the converter currents are proved to be flat outputs. Their reference can be used directly for feedforward, which shows the advantage of the flatness-based method that is also shown in previous publications.

To smooth out the transition response and limit the impact of the differential component in the feedforward path, a trajectory generation is added. With the help of the instantaneous power theory in the synchronous reference frame, the reference currents can be directly calculated from the active and reactive power references, which forms a PQ control structure via a current loop.

The rest of this paper is structured as follows. Section 2 analyses the control structure and control design method based on the flatness-based theory. Section 3 demonstrates the feasibility of the control structure by using real-time simulation. Finally, the conclusions are derived from the analysis of real-time simulation results.

2. Main research

2.1. Mathematical model of the three-phase four-wire converter

The three-phase four-leg voltage source converter is connected to the grid through a L filter, as depicted in Fig. 2. The internal resistance of the inductor is taken into account in this research.

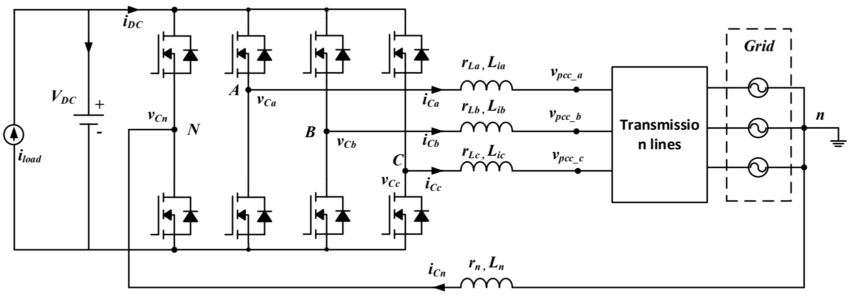

Fig. 2. Three-phase four-wire grid-connected converter.

The per-phase equivalent model of the system is shown in **Error! Reference source not found.**. Applying Kirchhoff's law yields in the Laplace domain.

$$\begin{bmatrix} v_{Ca} \\ v_{Cb} \\ v_{Cc} \end{bmatrix} = \begin{bmatrix} L_{ia} & 0 & 0 \\ 0 & L_{ib} & 0 \\ 0 & 0 & L_{ic} \end{bmatrix} \begin{bmatrix} si_{Ca} \\ si_{Cb} \\ si_{Cc} \end{bmatrix} + \begin{bmatrix} r_{La} & 0 & 0 \\ 0 & r_{Lb} & 0 \\ 0 & 0 & r_{Lc} \end{bmatrix} \begin{bmatrix} i_{Ca} \\ i_{Cb} \\ i_{Cc} \end{bmatrix}$$
$$+ L_n \begin{bmatrix} si_{Cn} \\ si_{Cn} \\ si_{Cn} \end{bmatrix} + r_n \begin{bmatrix} i_{Cn} \\ i_{Cn} \\ i_{Cn} \end{bmatrix} + \begin{bmatrix} v_{pcc\_a} \\ v_{pcc\_b} \\ v_{pcc\_c} \end{bmatrix} \begin{bmatrix} v_{Ca} \\ v_{Cb} \\ v_{Cc} \end{bmatrix}$$
$$= \begin{bmatrix} L_{ia} & 0 & 0 \\ 0 & L_{ib} & 0 \\ 0 & 0 & L_{ic} \end{bmatrix} \begin{bmatrix} si_{Ca} \\ si_{Cb} \\ si_{Cc} \end{bmatrix} + \begin{bmatrix} r_{La} & 0 & 0 \\ 0 & r_{Lb} & 0 \\ 0 & 0 & r_{Lc} \end{bmatrix} \begin{bmatrix} i_{Ca} \\ i_{Cb} \\ i_{Cc} \end{bmatrix}$$
$$+ L_n \begin{bmatrix} si_{Cn} \\ si_{Cn} \\ si_{Cn} \end{bmatrix} + r_n \begin{bmatrix} i_{Cn} \\ i_{Cn} \\ i_{Cn} \end{bmatrix} + \begin{bmatrix} v_{pcc\_a} \\ v_{pcc\_b} \\ v_{pcc\_c} \end{bmatrix} \quad (1)$$

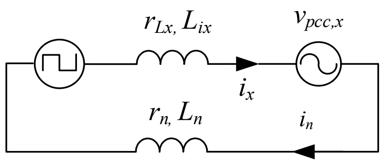

Where: x = A,B,C

Fig. 3. Per phase equivalent model of the system in the 0abc coordinate.

In which, v_{Ca}, v_{Cb}, v_{Cc} represent the terminal converter voltages; L_{ix}, L_n, r_{Lx}, r_n represent the line-side inductances and their internal resistances; $v_{pcc\_a}, v_{pcc\_b}, v_{pcc\_c}$ represent the phase-to-neutral voltages at the PCC.

Assuming that the three-phase inductors are balanced: $L_{ia} = L_{ib} = L_{ic} = L_n = L_i$ and $r_{La} = r_{Lb} = r_{Lc} = r_n = r_L$. The mathematical model in the *dq0* reference domain can be obtained as:

$$\begin{aligned}\begin{bmatrix} v_{Cd} \\ v_{Cq} \\ v_{C0} \end{bmatrix} &= \begin{bmatrix} L_i & 0 & 0 \\ 0 & L_i & 0 \\ 0 & 0 & 4L_i \end{bmatrix} \begin{bmatrix} si_{Cd} \\ si_{Cq} \\ si_{C0} \end{bmatrix} + \begin{bmatrix} r_L & 0 & 0 \\ 0 & r_L & 0 \\ 0 & 0 & 4r_L \end{bmatrix} \begin{bmatrix} i_{Cd} \\ i_{Cq} \\ i_{C0} \end{bmatrix} \\ &+ \begin{bmatrix} 0 & \omega L_i & 0 \\ -\omega L_i & 0 & 0 \\ 0 & 0 & 0 \end{bmatrix} \begin{bmatrix} i_{Cd} \\ i_{Cq} \\ i_{C0} \end{bmatrix} + \begin{bmatrix} v_{pcc\_d} \\ v_{pcc\_q} \\ v_{pcc\_0} \end{bmatrix} \begin{bmatrix} v_{Cd} \\ v_{Cq} \\ v_{C0} \end{bmatrix} \\ &= \begin{bmatrix} L_i & 0 & 0 \\ 0 & L_i & 0 \\ 0 & 0 & 4L_i \end{bmatrix} \begin{bmatrix} si_{Cd} \\ si_{Cq} \\ si_{C0} \end{bmatrix} + \begin{bmatrix} r_L & 0 & 0 \\ 0 & r_L & 0 \\ 0 & 0 & 4r_L \end{bmatrix} \begin{bmatrix} i_{Cd} \\ i_{Cq} \\ i_{C0} \end{bmatrix} \\ &+ \begin{bmatrix} 0 & \omega L_i & 0 \\ -\omega L_i & 0 & 0 \\ 0 & 0 & 0 \end{bmatrix} \begin{bmatrix} i_{Cd} \\ i_{Cq} \\ i_{C0} \end{bmatrix} + \begin{bmatrix} v_{pcc\_d} \\ v_{pcc\_q} \\ v_{pcc\_0} \end{bmatrix} \end{aligned} \tag{2}$$

where: $v_{Cd}, v_{Cq}, v_{C0} v_{Cd}, v_{Cq}, v_{C0}$ represent the converter voltages in the *dq0* domain.$i_{Cd}, i_{Cq}, i_{C0} i_{Cd}, i_{Cq}, i_{C0}$ represent the inductor currents in the *dq0* domain. $v_{pcc\_d}, v_{pcc\_q}, v_{pcc\_0} v_{pcc\_d}, v_{pcc\_q}, v_{pcc\_0}$ represent the phase-to-neutral PCC voltages in the dq0 domain.

The DC-link dynamic voltage can be given by:

$$C_{DC} \frac{dv_{DC}}{dt} = i_{Load} - i_{DC} C_{DC} \frac{dv_{DC}}{dt} = i_{Load} - i_{DC}$$
(3)

where: $C_{DC} C_{DC}$ represents the DC-link capacitance, $v_{DC} v_{DC}$ represents the DC-link voltage, and i_{DC}, i_{Load} represent the DC-link and load current.

The total active power of a three-phase system is given using the instantaneous power theory on synchronous reference frame [12]:

$$P_{AC} = \frac{3}{2}(v_{pcc\_d} i_{Cd} + v_{pcc\_q} i_{Cq}) P_{AC} = \frac{3}{2}(v_{pcc\_d} i_{Cd} + v_{pcc\_q} i_{Cq}) \tag{4}$$

Assuming in the condition of ideal grid voltages where $v_{pcc\_q} = 0$, (4) can be rewritten as:

$$P_{AC} = \frac{3}{2} v_{pcc\_d} i_{Cd} P_{AC} = \frac{3}{2} v_{pcc\_d} i_{Cd} \tag{5}$$

Neglecting the filter and converter losses the active power balance of the line side (P_{AC}) and DC side ($P_{DC} = v_{DC} i_{DC}$) gives:

$$i_{DC} = \frac{3}{2} \frac{v_{pcc\_d} i_{Cd}}{v_{DC}} i_{DC} = \frac{3}{2} \frac{v_{pcc\_d} i_{Cd}}{v_{DC}} \tag{6}$$

Finally, the DC link voltage dynamic is presented as:

$$C_{DC} \frac{dv_{DC}}{dt} = i_{Load} - \frac{3}{2} \frac{v_{pcc\_d} i_{Cd}}{v_{DC}} C_{DC} \frac{dv_{DC}}{dt} = i_{Load} - \frac{3}{2} \frac{v_{pcc\_d} i_{Cd}}{v_{DC}}$$
(7)

A similar derivation gives the reactive converter power:

$$Q = -\frac{3}{2} v_{pcc\_d} i_{Cq} Q = -\frac{3}{2} v_{pcc\_d} i_{Cq}$$
(8)

It can also be seen from (5) and (8) that the converter's active power injected/absorbed can be controlled by the d-axis current and the reactive power by the q-axis current of the PFC currents. This allows the converter to independently control the active and reactive power via reference currents in the synchronous reference frame. The dq-axis components of the reference currents can be calculated as:

$$i^*{}_{Cd} = \frac{2P_{ref}}{3v_{pcc\_d}} \tag{9}$$

$i^*{}_{Cd} = \frac{2P_{ref}}{3v_{pcc\_d}}$

$$i^*{}_{Cq} = -\frac{2Q_{ref}}{3v_{pcc\_d}} \tag{10}$$

$i^*{}_{Cq} = -\frac{2Q_{ref}}{3v_{pcc\_d}}$

Besides, the 0-axis current is always regulated to 0 to ensure no neutral current flows in the system, which makes the currents in the main three phases balanced.

2.2. Flatness-based control theory

Defining the system state $\underline{x} = \left[i_{Cd}, i_{Cq}, i_{C0}, v_{DC}\right]^T$ and the control input vector $\underline{u} = \left[v_{Cd}, v_{Cq}, v_{C0}\right]^T$, the state space (2) and (7) can be transformed into:

$$\frac{d}{dt}\underline{x} = \begin{bmatrix} \frac{-r_L}{L_i} i_{Cd} + \omega i_{Cq} + \frac{1}{L_i} v_{Cd} \\ \frac{-r_L}{L_i} i_{Cq} - \omega i_{Cd} + \frac{1}{L_i} v_{Cq} \\ \frac{-r_L}{L_i} i_{C0} + \frac{1}{4L_i} v_{C0} \\ \frac{-3v_{pcc\_d} i_{Cd}}{2v_{DC} C_{DC}} \end{bmatrix} + \begin{bmatrix} -\frac{v_{pcc\_d}}{L_i} \\ \frac{v_{pcc\_q}}{L_i} \\ \frac{-v_{pcc\_0}}{4L_i} \\ \frac{i_{Load}}{C_{DC}} \end{bmatrix} \tag{11}$$

$\frac{d}{dt}\underline{x} = \begin{bmatrix} \frac{-r_L}{L_i} i_{Cd} + \omega i_{Cq} + \frac{1}{L_i} v_{Cd} \\ \frac{-r_L}{L_i} i_{Cq} - \omega i_{Cd} + \frac{1}{L_i} v_{Cq} \\ \frac{-r_L}{L_i} i_{C0} + \frac{1}{4L_i} v_{C0} \\ \frac{-3v_{pcc\_d} i_{Cd}}{2v_{DC} C_{DC}} \end{bmatrix} + \begin{bmatrix} -\frac{v_{pcc\_d}}{L_i} \\ \frac{v_{pcc\_q}}{L_i} \\ \frac{-v_{pcc\_0}}{4L_i} \\ \frac{i_{Load}}{C_{DC}} \end{bmatrix}$

Defining the output vector:

$$\underline{y} = \begin{bmatrix} y_1 \\ y_2 \\ y_3 \end{bmatrix} = \begin{bmatrix} i_{Cq} \\ i_{C0} \\ v_{DC} \end{bmatrix} \tag{12}$$

$\underline{y} = \begin{bmatrix} y_1 \\ y_2 \\ y_3 \end{bmatrix} = \begin{bmatrix} i_{Cq} \\ i_{C0} \\ v_{DC} \end{bmatrix}$

To prove above system is a flat system, firstly the state vector $\underline{x} = \left[i_{Cd}, i_{Cq}, i_{C0}, v_{DC}\right]^T$ will be presented as a function of the flat outputs. By considering the load current as a disturbance, Eq. (7) can be simplified as:

$$\frac{dv_{DC}}{dt} = \dot{y}_3 = -\frac{3}{2}\frac{v_{pcc\_d} i_{Cd}}{C_{DC} y_3} \tag{13}$$

$\frac{dv_{DC}}{dt} = \dot{y}_3 = -\frac{3}{2}\frac{v_{pcc\_d} i_{Cd}}{C_{DC} y_3}$

The d-axis component of the inverter current can be written as:

$i_{Cd} = -\frac{2}{3}\frac{C_{DC}y_3\dot{y}_3}{v_{pcc\_d}} i_{Cd} = -\frac{2}{3}\frac{C_{DC}y_3\dot{y}_3}{v_{pcc\_d}}$

(14)

By using (12) and (14) the state vector of the system is given by:

$$\underset{\sim}{x} = \underset{\sim}{g}(y_1, y_2, y_3, \dot{y}_3)\underset{\sim}{x} = \underset{\sim}{g}(y_1, y_2, y_3, \dot{y}_3) \quad (15)$$

where

$$\underset{\sim}{g}(y_1, y_2, y_3, \dot{y}_3) = \begin{bmatrix} -\frac{2}{3}\frac{C_{DC}y_3\dot{y}_3}{v_{pcc\_d}}y_1 & y_2 & y_3 \end{bmatrix}^T \underset{\sim}{g}(y_1, y_2, y_3, \dot{y}_3) = \begin{bmatrix} -\frac{2}{3}\frac{C_{DC}y_3\dot{y}_3}{v_{pcc\_d}}y_1 & y_2 & y_3 \end{bmatrix}^T$$

The first two equations from Eq. (11) can be rewritten by neglecting the disturbances:

$$\underset{\sim}{u} = \begin{bmatrix} u_1 \\ u_2 \\ u_3 \end{bmatrix} = \begin{bmatrix} v_{Cd} \\ v_{Cq} \\ v_{C0} \end{bmatrix} = \begin{bmatrix} L_i\left(\frac{r_L}{L_i}i_{Cd} + \frac{di_{Cd}}{dt} - \omega i_{Cq}\right) \\ L_i\left(\frac{r_L}{L_i}i_{Cq} + \frac{di_{Cq}}{dt} + \omega i_{Cd}\right) \\ 4L_i\left(\frac{r_L}{L_i}i_{C0} + \frac{di_{C0}}{dt}\right) \end{bmatrix} \underset{\sim}{u} = \begin{bmatrix} u_1 \\ u_2 \\ u_3 \end{bmatrix} = \begin{bmatrix} v_{Cd} \\ v_{Cq} \\ v_{C0} \end{bmatrix} = \begin{bmatrix} L_i\left(\frac{r_L}{L_i}i_{Cd} + \frac{di_{Cd}}{dt} - \omega i_{Cq}\right) \\ L_i\left(\frac{r_L}{L_i}i_{Cq} + \frac{di_{Cq}}{dt} + \omega i_{Cd}\right) \\ 4L_i\left(\frac{r_L}{L_i}i_{C0} + \frac{di_{C0}}{dt}\right) \end{bmatrix} \quad (16)$$

Substituting Eq. (14) into Eq. (16) yields:

$$\underset{\sim}{u} = \begin{bmatrix} u_1 \\ u_2 \\ u_3 \end{bmatrix} = \begin{bmatrix} v_{Cd} \\ v_{Cq} \\ v_{C0} \end{bmatrix} = \begin{bmatrix} -\frac{2}{3}\frac{C_{DC}L_i}{v_{pcc\_d}}(\dot{y}_3.\dot{y}_3 + y_3.\ddot{y}_3) - \frac{2}{3}\frac{r_L C_{DC}}{v_{pcc\_d}}y_3.\dot{y}_3 - \omega L_i y_1 \\ -L_i\left(\dot{y}_1 - \frac{2}{3}\frac{C_{DC}}{v_{pcc\_d}}y_3.\dot{y}_3 + \frac{r_L}{L_i}y_1\right) \\ 4L_i(\frac{r_L}{L_i}y_2 + \dot{y}_2) \end{bmatrix}$$

$$\underset{\sim}{u} = \underset{\sim}{h}(y_1, \dot{y}_1, y_2, \dot{y}_2, y_3, \dot{y}_3, \ddot{y}_3)\underset{\sim}{u} = \begin{bmatrix} u_1 \\ u_2 \\ u_3 \end{bmatrix} = \begin{bmatrix} v_{Cd} \\ v_{Cq} \\ v_{C0} \end{bmatrix} = \begin{bmatrix} -\frac{2}{3}\frac{C_{DC}L_i}{v_{pcc\_d}}(\dot{y}_3.\dot{y}_3 + y_3.\ddot{y}_3) - \frac{2}{3}\frac{r_L C_{DC}}{v_{pcc\_d}}y_3.\dot{y}_3 - \omega L_i y_1 \\ -L_i\left(\dot{y}_1 - \frac{2}{3}\frac{C_{DC}}{v_{pcc\_d}}y_3.\dot{y}_3 + \frac{r_L}{L_i}y_1\right) \\ 4L_i(\frac{r_L}{L_i}y_2 + \dot{y}_2) \end{bmatrix}$$

$$\underset{\sim}{u} = \underset{\sim}{h}(y_1, \dot{y}_1, y_2, \dot{y}_2, y_3, \dot{y}_3, \ddot{y}_3) \quad (17)$$

It can be seen from Eqs. (15) and (17) that, the output vector satisfies the two conditions of a flat output vector of a flat system.

2.3. Flatness-based controller design

In the proposed control structure in Fig. 4, three controllers are designed in which the DC voltage regulator and the inner current controller are based on the flatness theory to achieve a fast dynamic response for the active power. In addition, the PCC voltage controller is utilized to regulate the reactive power rejected into the grid. The d-axis component and q-axis component of the reference are calculated from the required active and reactive power, which proves the advantage of the PQ control method.

The reference of the 0-axis current is set to zero to ensure that the three-phase system is balanced. The modulation index derived from the current controllers is applied to the 3D-SVM to generate the control signals for 8 switches of the 3P4W converter. In the flatness-based control, the system is driven towards the reference trajectory by a feed-forward signal and a reference generation. The feedback part is inserted only to eliminate the deviations caused by disturbances and other non-idealities.

As the system is near to the reference trajectory via feed-forward, thus linearizable around it, the feedback can be designed with linear methods even for nonlinear systems. Therefore, the linear controller design for each control loop is presented and the feed-forward part is determined in the next section.

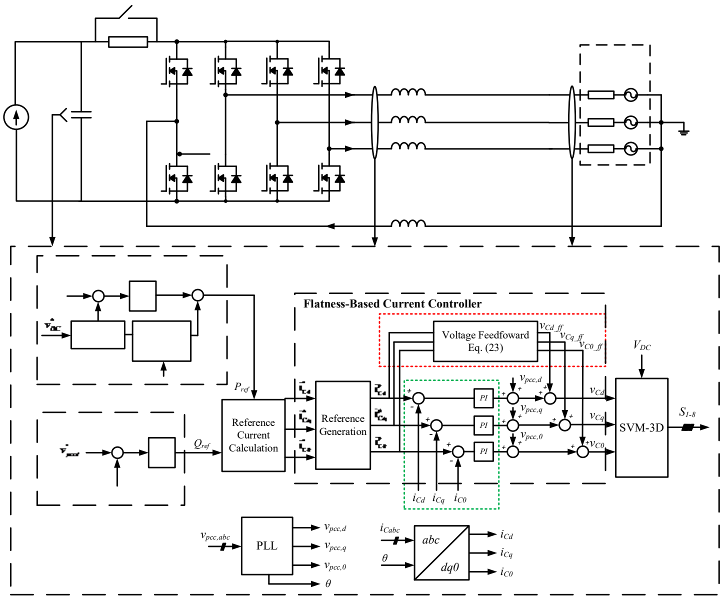

Fig. 4. PQ Control Structure using Flatness Theory.

2.3.1. Flatness-based DC voltage controller

From (14) the feed-forward component i_{Cd_ff} of the DC voltage controller can be directly derived from the reference DC-bus voltage v_{DC}^*:

$$i_{Cd\_ff} = \frac{2}{3}.\frac{C_{DC}\dot{v}_{DC}\dot{v}_{DC}^*}{v_{pcc\_d}} i_{Cd\_ff} = \frac{2}{3}.\frac{C_{DC}\dot{v}_{DC}\dot{v}_{DC}^*}{v_{pcc\_d}} \quad (18)$$

Applying the linearization method for the controller of the feed-back part: $i_{Cd} = I_{Cd} + \tilde{\imath}_{Cd}$,$v_{DC} = V_{DC} + \tilde{v}_{DC}$,$v_{pcc_d} = V_{pcc_d} + \tilde{v}_{pcc_d}$the transfer function from the output inverter current to the DC voltage can be presented as:

$$G_{vi} = \frac{\tilde{v}_{DC}}{\tilde{\iota}_{Cd}}\bigg|_{\tilde{v}_{pcc\_d}=0} = \frac{-1{,}5V_{pcc\_d}}{CV_{DC}s} G_{vi} = \frac{\tilde{v}_{DC}}{\tilde{\iota}_{Cd}}\bigg|_{\tilde{v}_{pcc\_d}=0} = \frac{-1{,}5V_{pcc\_d}}{CV_{DC}s} \tag{19}$$

Since the transfer function in (19) is an integral system, the PI controller $G_{cv}(s) = K_{pv} + \frac{K_{iv}}{s} G_{cv}(s) = K_{pv} + \frac{K_{iv}}{s}$ can be applied. The closed-loop of the DC voltage loop then is depicted as:

$$G(s) = \frac{G_{cv}(s)G_{vi}(s)}{1+G_{cv}(s)G_{vi}(s)} = \frac{1.5(\frac{K_{pv}V_{pcc\_d}}{C_{DC}V_{DC}}s+\frac{K_{iv}V_{pcc\_d}}{C_{DC}V_{DC}})}{s^2+1.5(\frac{K_{pv}V_{pcc\_d}}{C_{DC}V_{DC}}s+\frac{K_{iv}V_{pcc\_d}}{C_{DC}V_{DC}})} G(s) = \frac{G_{cv}(s)G_{vi}(s)}{1+G_{cv}(s)G_{vi}(s)}$$

$$= \frac{1.5(\frac{K_{pv}V_{pcc\_d}}{C_{DC}V_{DC}}s+\frac{K_{iv}V_{pcc\_d}}{C_{DC}V_{DC}})}{s^2+1.5(\frac{K_{pv}V_{pcc\_d}}{C_{DC}V_{DC}}s+\frac{K_{iv}V_{pcc\_d}}{C_{DC}V_{DC}})} \tag{20}$$

The parameters of the DC voltage parameters then are determined as:

$$\begin{cases} K_{pv} = \frac{(2\zeta\omega_n)(V_{DC}C_{DC})}{1{,}5V_{pcc\_d}} \\ K_{iv} = \omega_n^2 \frac{V_C C_{DC}}{1{,}5V_{pcc\_d}} \end{cases} \begin{cases} K_{pv} = \frac{(2\zeta\omega_n)(V_{DC}C_{DC})}{1{,}5V_{pcc\_d}} \\ K_{iv} = \omega_n^2 \frac{V_C C_{DC}}{1{,}5V_{pcc\_d}} \end{cases} \tag{21}$$

where ζ is the damping ratio and ω_n is the undamped natural frequency of a standard second-order transfer function.

Additionally, due to the appearance of the derivative component in the feed-forward part, the control signal may be clipped if a step reference is applied. A reference trajectory is therefore needed to smooth out the reference input value. Here in this design, a simple first-order low-pass filter is used to limit the derivative terms without influencing the computation time. Its transfer function can be described as:

$$G_{rg}(s) = \frac{y^p(s)}{y^*(s)} = \frac{\omega_c}{\omega_c + s} \tag{22}$$

where: ω_c denotes the cut-off frequency of the reference trajectory transfer function.

2.3.2. Flatness-based current controller

From Eq. (16) the feed-forward part $v_{Cd\_ff}, v_{Cq\_ff}, v_{C0\_ff}$ of the d-axis, q-axis and 0-axis current controller respectively can be directly derived:

$$\begin{cases} v_{Cd\_ff} = L_i \frac{d}{dt} i_{Cd}^* + r_L i_{Cd}^* - \omega L_i i_{Cq}^* \\ v_{Cq\_ff} = L_i \frac{d}{dt} i_{Cq}^* + r_L i_{Cq}^* + \omega L_i i_{Cd}^* \\ v_{C0\_ff} = 4L_i \frac{d}{dt} i_{C0}^* + 4r_L i_{C0}^* \end{cases} \tag{23}$$

For the controller design the feedback component, the transfer functions from the converter voltage to the converter current in the dq0 domain are determined from Eq. (2) by neglecting the PCC voltage disturbances:

$$\begin{cases} G_{vi\_d}(s) = \frac{i_{Cd}(s)}{v_{Cd}(s)} = \frac{1}{L_i s + r_L} \\ G_{vi\_q}(s) = \frac{i_{Cq}(s)}{v_{Cq}(s)} = \frac{1}{L_i s + r_L} \\ G_{vi\_0}(s) = \frac{i_{C0}(s)}{v_{C0}(s)} = \frac{1}{4(L_i s + r_L)} \end{cases} \tag{24}$$

Since the plant of the current loop is a first-order system, the PI controller $G_{cc} = K_{pc}(1 + 1/T_{ic}s)$ can be used to regulate the reference current. The time constant of the controller is chosen to be equal to the time constant T_{ic_d}, T_{ic_q}, and T_{ic_o} of the plant to eliminate the undesired pole of the plant:

$$T_{ic\_d} = T_{ic\_q} = T_{ic\_o} = \frac{L_i}{r_L} \quad (25)$$

The parameter K_p of the controller is determined as:

$$K_{pc\_d} = K_{pc\_q} = \frac{L_i}{T_{qd}}; K_{pc\_o} = \frac{4L_i}{T_{qd}} \quad (26)$$

where: T_{qd} is the settling time of the current loop.

Similar to the voltage controller design, the current reference generation using a low-pass filter is applied.

2.3.3. PCC voltage regulator

In low-voltage grids, the inverter injects power into the grid which causes a PCC voltage rise or drop that leads to many more severe power quality problems [19]. The active power injected/absorbed to/from the grid by the AC Battery as shown in Fig. 4 is controlled by the DC-link voltage controller. A control loop is needed to mitigate this issue. The PCC voltage, V_{PCC} is sensitive to both active and reactive power injected into the grid by the AC Battery. It can be expressed via Eq. (27) as:

$$\Delta V = \frac{P_C R_g + Q_C X_g}{V_g} \quad (27)$$

where: P_c, Q_c denotes the active and reactive power injected/absorbed to/from the grid, R_g, X_g denotes the resistance and impedance of transmission lines, and $\Delta V = V_g - V_{pcc}$ denotes the PCC voltage rise or drop caused by the power injected into the grid.

A PCC voltage controller therefore is required to regulate the PCC voltage. It can be done by controlling the reactive power injected into (or absorbed from) the grid by the storage device.

A simple control block diagram for the PCC voltage regulation is shown in Fig. 5. The AC voltage controller consists of a simple PI controller (or an integrator in this case) to calculate the reference reactive power for the inner control loop.

The fast-tracking performance of the flatness-based current control loop allows the controller to quickly adapt to changes in the q-axis component of the inverter current, which is used to directly regulate the PCC voltage. The plant model G(s) can be determined using Eq. (28):

$$V_{pcc,d} - V_{gd} = L_g \frac{di_{Cd}}{dt} - \omega L_g i_{Cq} + R_g i_{Cd} \quad (28)$$

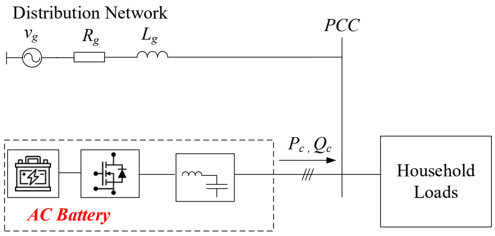

Fig. 5. Distribution network with the AC battery.

The open loop transfer function of the PCC voltage regulator can be then derived in the control diagram in Fig. 6. The controller design can be done using the magnitude optimization criterion or by pole-placement method.

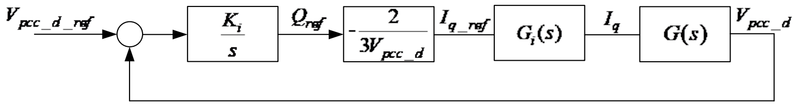

Fig. 6. PCC Voltage regulation block diagram.

3. Real-Time Simulation Verification

To quickly verify the FBC method for the three-phase four-wire converter with the proposed control design, a real-time simulation system based on the Hardware-in-the-loop (HIL) platform is conducted as shown in Fig. 7.

In this system, the three-phase four-wire converter in grid-connected mode is simulated by Typhoon HIL 402 while the program code for the control structure is embedded in the Digital Signal Processing (DSP) C2000 TMS320F28379D kit designed by Texas Instrument (TI). These two devices are connected through an interface board as shown in Fig. 7.

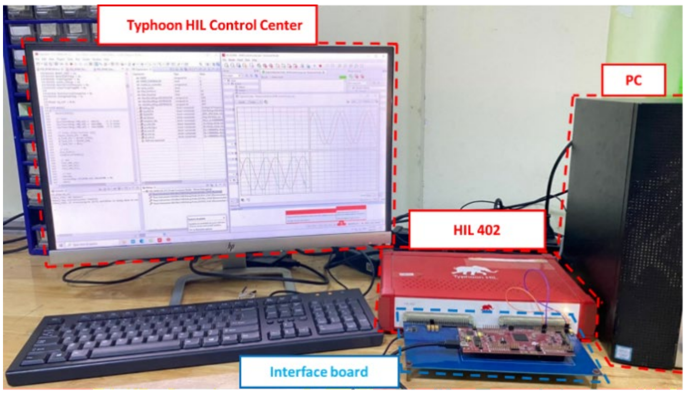

Fig. 7. Real-time simulation system with typhoon HIL.

The simulation results compare the dynamic response of the conventional current control method and the proposed method to illustrate the effectiveness of the Flatness-based control. The parameters of the system are given in **Error!**

Reference source not found.. Real-time simulation scenarios are shown in **Error! Reference source not found.**.

Table 1. Key specifications.

Parameter	Description	Value
V_{DC}	DC bus voltage (V)	650 ($\pm$10%)
V_{grid}	Line-line RMS PCC voltage (V)	380 ($\pm$10%)
f_0	Basic frequency (Hz)	50 ($\pm$1%)
f_{sw}	Switching frequency (kHz)	50
L_i	Filter inductance (μH)	330
r_L	Internal inductor resistance (Ω)	0.08
R_T	Resistance of transmission line	0.25
X_T	Inductance of transmission line	0.25

Table 1. Simulation scenario.

Phase	Time	Action
1	0 -3.5s	Charge DC-link capacitor via start-up resistors (R_{pre_charge}) in Fig. 4 to limit in-rush currents
2	3.5 - 3.6 s	Turning-on relay R_1 in Fig. 4
3	3.6 - 5.5 s	Enable PWM module and DC- voltage controller
4	5.75 - 6.5 s	Enable 11 kW DC-side load through a current source (Fig. 4)
5	6.5 – 9 s	Enable PCC voltage controller

Figure 8 illustrates the operation of the system in grid-connected mode. Firstly, in phase 1, all switches of the 3P4W converter are OFF and the relay in Fig. 4 is OFF, then the DC-link capacitor is naturally charged to around 537 V through the diode bridge and the start-up resistor of 30 Ω. The peak of the in-rush grid currents is limited at about 10 A in this phase as shown in Fig. 8(a). Then, in phase 2, the start-up resistor is bypassed by turning on relay R_1. A short time of 0.1 s is applied for this phase to avoid the inrush current. After that, at the beginning of phase 3, the DC-voltage controller and the PWM module are enabled. Continuously, to avoid the in-rush current in this phase, the reference of the DC voltage is ramped from 537 V to the final value of 650 V with the rate of 0.5 V/ms. A small peak of the grid currents of about 10 A is witnessed when starting the controller, then the DC-link voltage gradually tracks the reference voltage.

At the beginning of phase 4, a rated load of 11 kW suddenly changed with a step change of the current source at the DC side as shown in Fig. 8(c). With the proposed flatness-based control, the active power is rapidly achieved in Fig. 8(d); however, due to the effect of the transmission line impedance, the PCC voltage is reduced from 311 V to 305 V. Therefore, at the beginning of phase 5, the PCC voltage regulator is started, while the active power is kept at 11 kW, and about 12 kVAR of reactive power is controlled to compensate for the PCC voltage. After about 1s, the d-component of the PCC voltage returns to the initial value of 311 V as shown in Fig. 8(e).

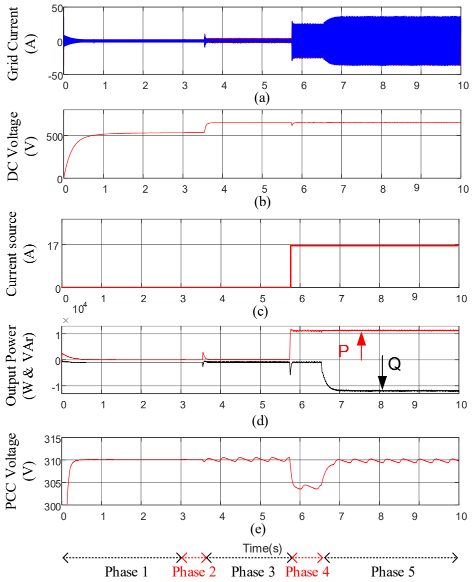

Fig. 8. System responses with Flatness-based control.

Furthermore, to verify the advantage of the flatness-based control, the dynamic responses are compared between the conventional control method and the Flatness-based control are compared in Figs. 9 and 10. While the DC-link voltage (V_{DC}), the active power (P), and the d-axis current (i_d) responses are depicted at the beginning of phase 4, the reactive power (Q) and q-axis current (i_q) responses are shown at the start of phase 5. The reference value is presented in a dashed blue line.

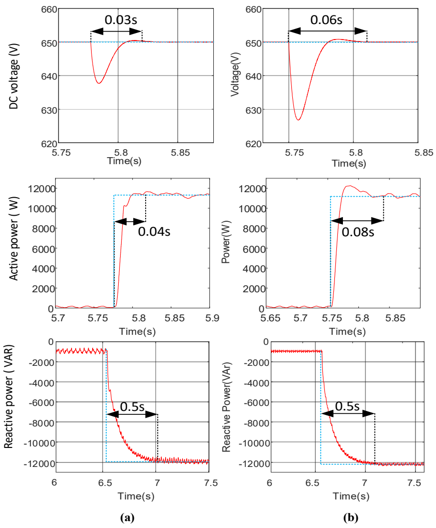

Fig. 9. Voltage and power responses comparison: (a) Proposed method, (b) Conventional method.

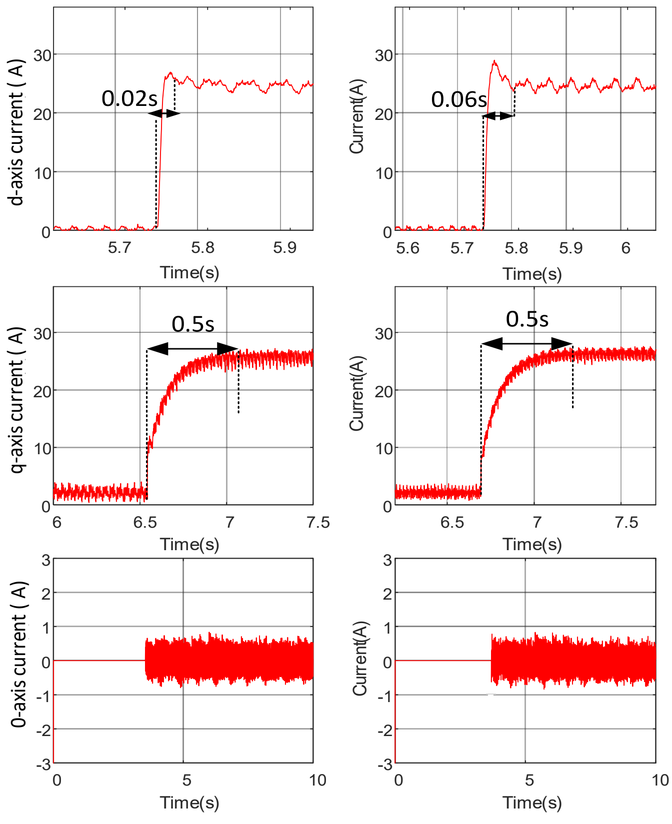

Fig. 10. Current responses comparison:
(a) Proposed method, (b) Conventional method.

With the flatness-based method, the dynamic responses yield better performance due to the planning trajectory with almost no overshoot compared to the conventional strategy. In detail, as summarized in Table 3, the nominal load is suddenly switched, and the decrease of DC voltage with the FBC method is just 12 V, while that with the conventional PI controller is double, at about 24 V. Moreover, the settling time of the DC voltage with the FBC method is also much smaller (approximately 1.5 times the grid period of 0.03 s) compared to 0.06 s of the conventional method.

The active power of the FBC method needs a shorter time to track the reference value, only 0.04 s (approximately 2 times the grid period), while that of the conventional method is double, 0.08 s. While no overshoot is shown in the power with the FBC method, there is an overshoot of about 1.5 kW in active power with the PI controller. The response time for the reactive power of both control methods is similar because the same PI controller is applied for the PCC voltage regulator for both cases.

Table 2. Transient-response specification.

Criteria	Parameter	Flatness-based Control	Conventional Control
V_{DC}	Voltage drop (%)	1.84	3.54
	Settling time (s)	0.03 (~1.5 T)	0.06 (~3 T)
P	Overshoot (%)	0	13.6
	Settling time (s)	0.04 (~2 T)	0.08 (~4 T)
Q	Overshoot (%)	0	0
	Settling time (s)	0.5	0.5
i_d	Overshoot (%)	0	5
	Settling time (s)	0.02 (~1 T)	0.06 (~3 T)
i_q	Overshoot (%)	0	0
	Settling time (s)	0.5	0.5

where T indicates the grid period.

Furthermore, the current responses of the proposed method for the 3P4W converter are compared to those of the conventional method as shown in Fig. 10. The d-axis current of the FBC method needs a shorter time to track the reference value, only 0.02 s (approximately the grid period), while that of the conventional method is about triple. No overshoot is shown in the d-axis current response in Fig. 10 with the FBC method, while there is an overshoot of about 5 A in the d-axis current with the PI controller. Besides, the response time for the q-axis current of both the proposed method and conventional methods are similar because the same PI controller is applied for the PCC voltage regulator for both cases. Finally, the current on the 0-coordinate is kept around 0 to guarantee that the three-phase system is balanced.

An important note is that the proposed FBC improves the dynamic responses compared to the conventional method. In the steady state, both two control methods give the same performance of the grid current, and Total Harmonics Distortion (THD) is just 1.1% as shown in Fig. 11, which meets the IEEE 519 standard.

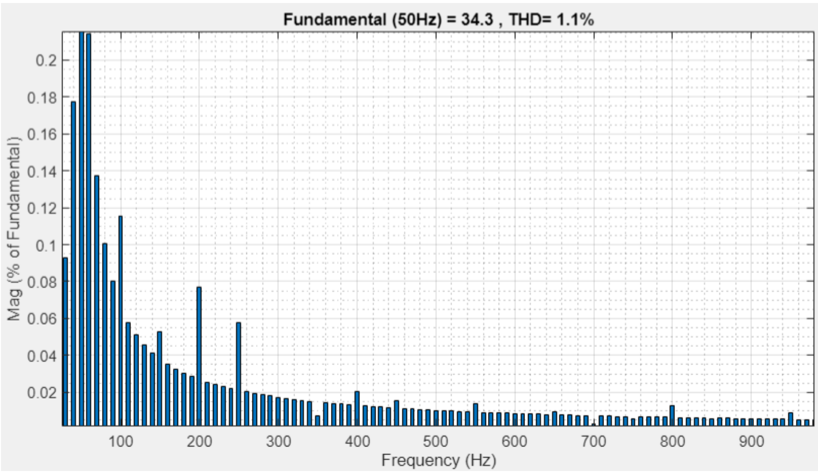

Fig. 11. THD grid current in steady-state phase.

4. Conclusion

In this paper, a PQ control strategy via current control based on Flatness theory has been proposed for a three-phase four-wire inverter of an AC Battery in grid-tied mode. The active and reactive power are shown to be independently regulated via the current loop using instantaneous power theory in the synchronous reference frame. Hence, a multi-functional energy storage system is designed with the ability to regulate both DC-link voltage and PCC voltage, in which the fast dynamic response is achieved due to the advantage of the FBC method.

Real-time simulation is carried out the performance of the proposed method is superior to that of the conventional method. These results verify the effectiveness of the proposed control design and the feasibility of experimental implementation. Furthermore, the regulation for the harmonic distortion for the PCC voltage would be presented in future work based on the idea for harmonic detection and reduction presented in [10] for a 1-phase system.

Acknowledgments

This research is funded by the Hanoi University of Science and Technology (HUST) under project number T2022-TĐ-001.

References

1. Kang, M.-S.; Park, Y.-K.; and Kim, K.-T. (2020). Economic feasibility through the optimal capacity calculation model of an energy storage system connected to solar power generator. *Energy & Environment*, 31(5), 860-869.
2. Zhu J-H; Ren H; Zhang X; Zhang L; Zhang P.; and Li, H. (2022). Two-level optimization model of hybrid energy storage system in wind/solar distributed generation system. *Transactions of the Institute of Measurement and Control*, 014233122211423.
3. Hocine, L.; Menaa, M.; and Yazid, K. (2021). Sensorless control of wind power generator with flywheel energy storage system. *Wind Engineering*, 45(2), 257-277.
4. Hossain, E.; Murtaugh, D.; Mody, J.; Faruque, H.M.R.; Sunny, M.S.H.; and Sami, N.M. (2019). A comprehensive review on second-life batteries: Current state, manufacturing considerations, applications, impacts, barriers & potential solutions, business strategies, and policies. *IEEE Access*, 7(1), 73215-73252.
5. Bai, J. (2019). Multi-function energy storage system for smart grid. *Proceedings of the* 2019 *IEEE Green Energy and Smart Systems Conference* (*IGESSC*), Long Beach, CA, USA, 1-4.
6. Singh, Y.; Singh, B.; and Mishra, S. (2020). Multifunctional control for PV-integrated battery energy storage system with improved power quality. *IEEE Transactions on Industry Applications*, 56(6), 6835-6845.
7. Deng, W.; and Dai, C. (2022). A multifunctional energy storage system with fault-tolerance and its hierarchical optimization control in AC-Fed railways. *IEEE Transactions on Power Delivery*, 37(4), 2440-2452.
8. Yang, P.; Ming, W.; Liang, J.; Ugalde-Loo, C.E.; Navaratne, R.; Ellabban, O.; Ludtke, I. (2022). SiC-based improved neutral legs with reduced capacitors for three-phase four-wire EV chargers. *IEEE Transactions on Transportation Electrification*, 8(2), 2565-2582.

9. Verma, A.; Singh, B.; Chandra, A.; and Al-Haddad, K. (2018). An implementation of solar PV array based multifunctional EV charger. *Proceedings of the* 2018 *IEEE Transportation Electrification Conference and Expo (ITEC)*, Long Beach, CA, USA, 531-536.
10. Taghizadeh, S.; Hossain, M.J.; Lu, J.; and Water, W. (2018). A unified multi-functional on-board EV charger for power-quality control in household networks. *Applied Energy*, 215, 186-201.
11. Varma, R.K.; and Siavashi, E.M. (2018). PV-STATCOM: A new smart inverter for voltage control in distribution systems. *IEEE Transactions on Sustainable Energy*, 9(4), 1681-1691.
12. Chen, M.-R.; Wang, H.; Zeng, G.-Q.; Dai, Y.-X. and Bi, D.-Q. (2018). Optimal P-Q control of grid-connected inverters in a microgrid based on adaptive population extremal optimization. *Energies*, 11(8), 2107.
13. Scalcon, F.P.; Fang, G.; Vieira, R.P.; Gründling, H.A.; and Emadi, A. (2022). Discrete-time super-twisting sliding mode current controller with fixed switching frequency for switched reluctance motors. *IEEE Transactions on Power Electronics*, 37(3), 3321-3333.
14. Shami, T.M.; El-Saleh, A.A.; Alswaitti, M.; Al-Tashi, Q.; Summakieh, M.A.; and Mirjalili, S. (2022). Particle swarm optimization: A comprehensive survey. *IEEE Access*, 10, 10031-10061.
15. Chowdhury, V.R.; and Divan, D. (2021). Feedback Linearization based Direct Power Control of a three-phase grid-connected inverter with online parameter update. *Proceedings of the* 2021 *IEEE Energy Conversion Congress and Exposition* (*ECCE*), Vancouver, BC, Canada, 1073-1078.
16. Alqatamin, M.; McIntyre, M.L.; and Latham, J. (2019). Backstepping control for single-phase grid-connected inverter utilizing variable structure observer. *Proceedings of the* 2019 *American Control Conference* (*ACC*), Philadelphia, PA, USA, 646-651.
17. Greeff, M.; and Schoellig, A.P. (2018). Flatness-based model predictive control for quadrotor trajectory tracking. *Proceedings of the* 2018 *IEEE/RSJ International Conference on Intelligent Robots and Systems (IROS)*, Madrid, Spain, 6740-6745.
18. Mikram, O.; Abouloifa, A.; Lachkar, I.; Aourir, M.; and Katir, H. (2020). Flatness-based-control of three-phase shunt active power filters based on five-level NPC inverter. *Proceedings of the* 2020 *International Conference on Electrical and Information Technologies* (*ICEIT*), Rabat, Morocco, 1-5.
19. Ahmad, S.; Jhuma, U.K.; Karimi, M.; Pourdaryaei, A.; Mekhilef, S.; Mokhlis, H.; and Kauhaniemi, K. (2022). Direct power control based on point of common coupling voltage modulation for grid-tied AC microgrid PV inverter. *IEEE Access*, 10, 109187-109202.